Chemical Engineering Science 317 (2025) 122003

Contents lists available at ScienceDirect

Chemical Engineering Science

journal homepage: www.elsevier.com/locate/ces

A novel reduced order model of circulating fluidized beds coupled with enhanced compressed sensing and temporal convolutional neural networks

Xiaofei Li [a], Shuai Wang [a,b], Kun Luo [a,b,*], Jianren Fan [a,b]

[a] State Key Laboratory of Clean Energy Utilization, Zhejiang University, Hangzhou 310027, China
[b] Shanghai Institute for Advanced Study of Zhejiang University, Shanghai 200120, China

ARTICLE INFO

Keywords:
Circulating fluidized bed
Reduced order model
Proper orthogonal decomposition
Compressed sensing
Digital twin

ABSTRACT

Industries urge an online in-time prediction for the simulation of chemical engineering processes. The circulating fluidized bed (CFB), as a complex multiphase reactive flow device, cannot be predicted in real-time using existing experimental and computational fluid dynamics (CFD) methods. In this work, a novel reduced order model (ROM) coupled with enhanced compressed sensing (ECS) and temporal convolutional neural networks (TCN) is developed to fulfill the goal, which relies on data from limited measurements to achieve real-time early warning function. Specifically, the key variables of dense gas–solid flow are decomposed into orthogonal modes of different orders and their corresponding mode coefficients. Based on this, a mapping relationship is established between the current measurement data and the mode coefficients at future time steps. The predictive error of the ECS-TCN-ROM developed in this study remains below 20% for most of the time across different variables, with the online prediction efficiency of a single variable being 25,000 times that of traditional CFD. This ECS-TCN-ROM lays the foundation for the digital twin of CFB.

1. Introduction

In recent years, significant efforts have been made to develop an energy supply system dominated by clean and low-carbon sources to achieve carbon peak and neutrality goals. This includes promoting the clean and efficient use of coal, reducing environmental pollution, and diversifying the energy mix. One of the key technologies for achieving these objectives is the efficient and low-carbon utilization of fluidized bed systems. However, the complex multiphase reactive flows within fluidized beds involve numerous interactions—between particles and fluids, particles and particles, and particles and walls—along with coupled phenomena such as heat transfer, mass transfer, and chemical reactions (Wang et al., 2020; Zhong et al., 2016; Wang et al., 2018). These complexities pose significant challenges for experimental measurements and system optimization. Computational fluid dynamics (CFD)-based methods often require complex iteration to capture the particle transient behaviors and collisions of particles, which is computationally expensive and cannot meet the needs of real-time simulation in some industrial applications. Therefore, existing experimental measurements and CFD methods exhibit limitations in accurately and efficiently sensing the state within fluidized beds, failing to meet the stringent demands of modern power systems for efficient and rapid response in coal-fired power plants. The advancement of technologies such as artificial intelligence and big data has made real-time simulation and prediction of multiphase flow dynamics in fluidized beds possible by linking physical systems with their digital counterparts. By creating a digital twin (DT) of the reactor, real-time data from the physical space can be fed into a virtual model for efficient prediction, providing actionable insights for industrial applications. The construction of the DT system imposes higher demands on prediction speed and the integration of physical and digital space.

As for the prediction speed, reduced order model (ROM) was proposed to address this challenge. (Yang et al., 2024; Chen et al., 2025; Hajisharifi et al., 2023). Proper orthogonal decomposition (POD) is one of the representatives of ROM. POD decomposes the full order model (FOM) field dataset obtained in the first phase of the ROM framework into a series of main spatial modes and their corresponding mode coefficients. The spatial modes are fixed and do not change with variations in the timestep. By selecting an appropriate number of spatial modes based on the flow field characteristics (the energy associated with each mode), the flow field can be reconstructed within an acceptable error margin. Based on whether the mode coefficients are calculated under the CFD control equation framework, POD-based ROM can be divided into

---

* Corresponding author at: State Key Laboratory of Clean Energy Utilization, Zhejiang University, Hangzhou 310027, China.
E-mail address: zjulk@zju.edu.cn (K. Luo).

https://doi.org/10.1016/j.ces.2025.122003
Received 13 May 2025; Received in revised form 6 June 2025; Accepted 7 June 2025

Nomenclature

$A_{p,i}$	particle surface area, m^2
B	measurement point position matrix
C_V	particle specific heat capacity, J/(kg·K)
D	dilation vector
D_g	turbulent mass diffusion coefficient
D_p	drag force coefficient
E	energy proportion
f	particle distribution function
f_D	particle distribution function at local equilibrium
f_G	particle distribution function in this state
f_{sg}	Savitzky-Golay function
f_{TCN}	temporal convolutional neural network function
g	gravitational acceleration, m/s^2
h_g	enthalpy of gas, J/kg
K	kernel size
m_p	particle mass, kg
$\mathrm{Nu}_{g,p}$	Nusselt number
P	column permutation matrix
p	pressure, Pa
Q	unitary matrix
$\dot{Q}$	energy source term, $J/(s \cdot m^3)$
Q_{fp}	heat source term, $J/(s \cdot m^3)$
r_p	particle radius, m
R	upper triangular matrix
R_{field}	receptive field
S	inter-phase momentum exchange term, $kg/(m^2 \cdot s^2)$
S_h	inter-phase energy exchange term, $J/(s \cdot m^3)$
T_g	gas temperature, K
T_p	particle temperature, K
T_w	wall temperature, K
u_g	gas velocity, m/s
u_p	particle velocity, m/s
U	left singular vector
V	right singular vector
W	spatial–temporal matrix
$W_0(x)$	time mean value of the target variable
$Y_{g,i}$	mass fraction of species
X	FOM data
Y	measurement data

Acronyms

AE	autoencoder
ANN	artificial neural networks
CFB	circulating fluidized bed
CFD	computational fluid dynamics
CNN	convolutional neural network
CS	compressed sensing
DEIM	discrete empirical interpolation method
DMD	dynamic mode decomposition
DNN	deep neural network
DT	digital twin
ECS	enhanced compressed sensing
FOM	full order model
KLT	Karhunen–Loève transform
LSTM	long short-term memory network
MP-PIC	multi-phase particle-in-cell
PCA	principal component analysis
PDF	particle distribution function
POD	proper orthogonal decomposition
RBF	radial basis function
ROM	reduced-order model
S-G	Savitzky-Golay
SVD	singular value decomposition
SVR	support vector regression
TCN	temporal convolutional neural network

Greek symbols

α^{input}	input coefficient vector of prediction
α^{output}	output coefficient vector of prediction
$\alpha_k(t)$	POD coefficient
α_p	particle acceleration, m/s^2
$\delta \dot{m}_{i,chem}$	chemical source term, kg
$\dot{\delta m}_p$	change in gas mass, kg
κ_g^{eff}	effective gas thermal conductivity, W/(m·K)
ε_g	gas volumn fraction
ε_p	particle volumn fraction
ε_{cp}	maximum packing density
ρ_g	gas density, kg/m^3
σ	Stefan-Boltzmann constant
τ_g	effective stress tensor, Pa
τ_D	particle collision relaxation time
τ_G	particle collision relaxation time in this state
τ_p	particle collision stress, Pa
μ_g	fluid viscosity, kg/(m·s)
λ_k	the eigenvalue
Σ	matrix of singular values
Θ	transformation matrix
Ψ	mode matrix
φ	viscous dissipation, $J/(s \cdot m^3)$
Φ_k	POD mode
χ_j	judgment matrix

Subscripts

g	gas phase
k	order of modes
p	particle phase
w	wall

two categories: intrusive ROM and non-intrusive ROM. Compared with intrusive ROM, non-intrusive ROM directly utilizes surrogate models such as artificial neural networks (ANN) and other methods to predict coefficients (Li et al., 2022). This method is simple to implement and has strong stability (Li et al., 2024). Due to the high code complexity and the numerical issues of the intrusive ROM, this study focuses on non-intrusive ROM. The ROM has been successfully utilized in various fields, including fire prediction (Cheng et al., 2022), combustion (Aversano et al., 2021), and proton exchange membrane batteries (Ansari, 2023). This approach replaces the high-dimensional system with a low-dimensional representation through projection and machine learning, significantly reducing both the complexity of the original system and the associated computational costs. For example, Lumley et al. (Berkooz et al., 1993) first introduced it to identify the coherent structures of turbulent flows. Li et al. (Li et al., 2022; Li et al., 2024) coupled POD with radial basis function (RBF) and long short-term memory neural networks (LSTM) to predict the transient bed characteristics in both spouted and bubbling fluidized beds, validating the effectiveness of the POD-based ROM. Hajisharifi et al. (Hajisharifi et al., 2023; Hajisharifi et al., 2024) combined POD with LSTM to construct a ROM, extending the reduced-order approach to Lagrangian fields. Fang et al. (Fang et al., 2024) coupled the POD method with bidirectional LSTM and developed a ROM to capture the complex spatiotemporal modes of the fluidized bed, achieving higher accuracy compared to traditional LSTM and ANN. Li et al. (Li et al., 2024; Li et al., 2024) employed POD and temporal convolutional networks (TCN) to construct ROMs for the Eulerian and Lagrangian variables during the flow and heat transfer processes in bubbling fluidized beds, further verifying the accuracy and efficiency of the ROM. Xu et al. (Xu et al., 2024) utilized POD and support vector regression (SVR) to build a ROM for a corner-cut circular coal-fired boiler. Then, they combined a control algorithm with a particle swarm optimization technique to optimize coal and air distribution, reducing the corrosion rate of the water wall from 36.34 % to 10.04 %. Additionally, spectral POD and multi-scale POD have been applied to fluidized beds to further enhance ROM accuracy (Zarepour et al., 2024; Chen et al., 2025). Although substantial work has been done for the ROM, previous research has primarily focused on pure simulation processes, without integrating them with real fluidized beds. Furthermore, with regard to the inputs for ROM, most studies on transient flow field prediction have not considered the insufficient availability of rich information in actual fluidized beds. Compressed sensing (CS) offers a promising solution to address these challenges. In the CS framework, several greedy algorithms have been proposed to determine the measurement point locations, such as the QR decomposition with column pivoting (QR-pivoting) (Businger and Golub, 1965) and the discrete empirical interpolation method (DEIM) (Barrault et al., 2004; Sargsyan et al., 2015). The full-state flow field in digital space can be reconstructed and predicted from sparse measurements in physical space by combining the CS and the ROM. For example, Bright et al. (Bright et al., 2013) reconstructed the pressure field and Reynolds number around the cylinder through pressure sensor measurements on the cylinder by CS-ROM. Gomes et al. (Gomes et al., 2024) combined optimal sensor placement with convolutional neural networks, achieving 95.5 % accuracy in flow field reconstruction using 1,000 sensors in a lid-driven cavity flow. Zhao et al. (Zhao et al., 2021) used the CS-ROM to reconstruct lift and moment in a typical subsonic turbulent flow experiment using 4 to 8 measurement points. Rao (Rao pp. , 2024) applied CS-ROM in single-phase heat transfer processes to back-estimate flow states. Based on a limited number of pressure measurements, they accurately identified the Mach number, Reynolds number, and angle of attack around an airfoil. Yang et al. (Yang and Ma, 2024) further analyzed the impact of sparse bases derived from discrete Fourier transform, discrete cosine transform, and POD on reconstruction performance. The results demonstrated that the POD-based method outperforms the other two methods in terms of accuracy. Jayaraman et al. (Jayaraman and Mamun, 2020) applied the DEIM and QR-pivoting methods to construct compressed sensing for flow fields and found that the DEIM outperforms the QR-pivoting method in terms of accuracy. Additionally, non-orthogonal modes tend to suffer from ineffective sensor placement and high algorithmic complexity. For multiphase flow, Jiang et al. (Jiang et al., 2022) applied the CS-ROM to the steam turbine and realized the transient temperature field reconstruction. Procacci et al. (Procacci et al., 2022) combined POD and the QR-pivoting to construct a DT of a parametric steady combustion process. The study identified the optimal sensor placement that minimizes prediction error and successfully predicted the distribution of reacting scalars using a limited number of measurements. Building on this, Procacci et al. (Procacci et al., 2024) reconstructed the three-dimensional chemical field of flames from chemiluminescence signals. Compared to traditional methods requiring multiple views, the approach only requires a single view to reconstruct the chemiluminescence field. Menges et al. (Menges et al., 2024) proposed an algorithmic framework for real-time state monitoring and prediction using multivariate ship engine thermal imaging data. Real-time prediction of engine temperature fields can be realized by combining POD, optimal sampling locations, and dynamic mode decomposition (DMD). Some studies combined non-POD ROMs and the CS have been reported. Nair et al. (Nair and Goza, 2020) proposed a neural network framework to learn the nonlinear relationship between the sensor measurements and the reduced space state. The framework can be incorporated with the linear subspace (such as POD-ROM) and the nonlinear manifold. Luo et al. (Luo et al., 2023) combined CS and autoencoder (AE) to reconstruct the flow field using sensor data. This method yielded excellent results in simulating the flow around both a circular and a square cylinder. In the study of Zhang et al. (Zhang et al., 2022), LSTM was used for modeling the sensor measurement evolution. The flow field was subsequently reconstructed using sensor measurements based on DMD and DNN. Loiseau et al. (Loiseau et al., 2018) proposed a general dynamic ROM framework based on the sparse identification of nonlinear dynamics and applied it to the transient and post-transient laminar cylinder wake. Most of the above studies focus on single-phase flow and simple chemical reactions, with further extension needed in large reactors with multiphase and multi-field coupling. Although the current CS method strives to capture the most detailed flow field information using the least sensor data, the accuracy of this method still needs to be improved. In addition, the current mainstream methods for CS mainly focus on the reconstruction of the flow field at the current time. There are few reports on predicting the flow field in the future. In industrial applications, it is necessary not only to utilize sparse data to obtain the flow field at the current momentbut also to predict the future flow field as much as possible, to facilitate early warning and timely control of dangerous conditions that may occur in the production process.

To advance the above concept, this work develops a novel enhanced CS-TCN-ROM (ECS-TCN-ROM) for multiphase reactive flows, aiming to overcome the computational limitations of traditional CFD methods, enabling the realization of a rapid prediction platform that integrates real-time data from the physical space in multiphase reactive flow processes. The model is applied to fast predict hydrodynamics and thermochemical characteristics of an industrial-scale circulating fluidized bed (CFB) boiler. The remainder of this article is listed as follows. Section 2 describes the research methods, including FOM and ECS-TCN-ROM. Section 3 outlines the numerical settings for the industrial-scale CFB boiler. Section 4 presents the results and discussion of the ECS-TCN-ROM, including POD analysis, ECS, coefficient prediction, and flow field reconstruction. The concluding remarks are presented in the final section.

2. Methodology

Section 2.1 presents the FOM computational method. Section 2.2 introduces the ECS-TCN-ROM model, including mode decomposition, enhanced compressed sensing, time coefficient prediction, and flow field reconstruction.

2.1. Full order model

In this study, the FOM simulations are calculated using the multiphase particle-in-cell (MP-PIC) method. The MP-PIC method employs the concept of parcels, which groups the original particles into a numerical parcel, and simplifies particle–particle collisions by introducing a solid stress model. This approach enables the analysis of dense gas–solid systems at large scales with a reasonable number of computational particles, making the MP-PIC method highly promising for simulating both pilot-scale and industrial-scale CFB. Therefore, in this study, the MP-PIC method is adopted as a reliable dataset for the ROM. The fluid phase is solved by Navier-Stokes equations, while a particle distribution function (PDF) is introduced for the particle phase. The governing equations for the MP-PIC method have been well documented in previous publications (Wang et al., 2018). The focus of this study is on the ROM, while the FOM is responsible for providing data to the ROM. Therefore, the governing equations of the FOM are outlined in Table 1.

The chemical reactions in the FOM are based on the public literature (Xie et al., 2017), with a set of 28 homogeneous and heterogeneous reactions selected to represent the chemical reactions in the CFB boiler. The volatile combustion, coke combustion, and pollutant formation are incorporated into the chemistry model. Similar to the governing

Table 1
Governing equations for the FOM.

Gas phase

Mass conservation equation:

$$\frac{\partial(\varepsilon_g\rho_g)}{\partial t} + \nabla\cdot(\varepsilon_g\rho_g u_g) = \delta\dot{m}_p \tag{1}$$

Momentum conservation equation:

$$\frac{\partial(\varepsilon_g\rho_g u_g)}{\partial t} + \nabla\cdot(\varepsilon_g\rho_g u_g u_g) = -\varepsilon_g\nabla p + \nabla\cdot(\varepsilon_g\tau_g) + \rho_g\varepsilon_g g + S \tag{2}$$

Energy conservation equation:

$$\frac{\partial}{\partial t}(\varepsilon_g\rho_g h_g) + \nabla\cdot(\varepsilon_g\rho_g h_g u_g) = \varepsilon_g\left(\frac{\partial p}{\partial t} + u_g\cdot\nabla p\right) + \varphi - \nabla\cdot(\varepsilon_g q) + \dot{Q} + S_h + \dot{q}_D \tag{3}$$

Species conservation equation:

$$\frac{\partial(\varepsilon_g\rho_g Y_{g,i})}{\partial t} + \nabla\cdot(\varepsilon_g\rho_g Y_{g,i} u_g) = \nabla\cdot(\rho_g D_g\varepsilon_g\nabla Y_{g,i}) + \delta\dot{m}_{i,chem} \tag{4}$$

Gas stress tensor:

$$\tau_{g,ij} = \mu_g\left(\frac{\partial u_i}{\partial x_j} + \frac{\partial u_j}{\partial x_i}\right) - \frac{2}{3}\mu_g\delta_{ij}\frac{\partial u_k}{\partial x_k} \tag{5}$$

Interphase momentum exchange term:

$$S = -\iiint f\left\{m_p\left[D_p(u_g - u_p) - \frac{\nabla p}{\rho_p}\right] + u_p\frac{dm_p}{dt}\right\}dm_p du_p dT_p \tag{6}$$

Energy exchange term:

$$S_h = \iiint f\left\{m_p\left[D_p(u_p - u_g)^2 - C_V\frac{dT_p}{dt}\right] - \frac{dm_p}{dt}\left[h_p + \frac{1}{2}(u_p - u_g)^2\right]\right\}dm_p du_p dT_p \tag{7}$$

Solid phase

Particle density function (PDF):

$$\frac{\partial f}{\partial t} + \frac{\partial(f u_p)}{\partial x} + \frac{\partial(f\alpha_p)}{\partial u_p} = \frac{f_D - f}{\tau_D} + \frac{f_G - f}{\tau_G} \tag{8}$$

Particle acceleration:

$$\alpha_p = \frac{du_p}{dt} = D_p(u_g - u_p) - \frac{\nabla p}{\rho_p} - \frac{\nabla\tau_p}{\varepsilon_p\rho_p} + g + F_p \tag{9}$$

Particle volume fraction:

$$\varepsilon_p = \iiint f\frac{m_p}{\rho_p}dm_p du_p dT_p \tag{10}$$

Contact normal stress of the particle:

$$\tau_p = \frac{P_p\varepsilon_p}{max[(\varepsilon_{cp} - \varepsilon_p), \delta(1 - \varepsilon_p)]} \tag{11}$$

Energy conservation equation of particle:

$$m_p C_V\frac{dT_p}{dt} = \frac{\kappa_g^{eff}\mathrm{Nu}_{g,p}}{2r_p}A_p(T_g - T_p) + A_p\varepsilon_p\sigma(T_w^4 - T_p^4) - \Delta H_{rs} \tag{12}$$

equations, the chemical reactions are not elaborated upon. The chemical reaction equations are listed in Table S1 of Supporting Information, and the chemical reaction rates and mechanisms can be referred to the previous publications (Xie et al., 2017; Ku et al., 2015).

2.2. Reduced order model

In this study, the decomposition process utilizes the proper orthogonal decomposition (POD) method, which is also referred to as principal component analysis (PCA) or the discrete Karhunen-Loève transform (KLT) (Li et al., 2024). As shown in Fig. 1, based on the CFD snapshot data, POD decomposes the flow field into dominant spatial modes and their corresponding temporal coefficients. The modes are sorted from high to low according to the energy and the eigenvalue corresponding to the modes. ECS is used to construct the mapping between the physical space and the digital space. The time coefficients rely on the TCN for online real-time prediction. Finally, a fast prediction ECS-TCN-ROM model based on real physical measurement data is developed, which can be applied to multiphase reactive flow industry research. The offline preparation relies on the FOM, which incorporates physical constraints. Intuitively, the online prediction phase does not directly account for these physical constraints, as data and mathematical calculations primarily drive it. However, the modes and corresponding coefficients derived from proper orthogonal decomposition (POD) in the offline stage inherently respect these physical constraints.

2.2.1. Proper orthogonal decomposition

Singular value decomposition (SVD) is implemented in POD for mode decomposition. The spatial–temporal snapshot matrix of a FOM can be regarded as ($M \times N$), where M represents the spatial dimension, i.e., the number of grids. N represents the temporal dimension, i.e., the number of time snapshots. Performing SVD decomposition on the FOM matrix yields:

$$W = U\Sigma V^T \tag{13}$$

where U is the spatial mode and V is the time mode. Σ is the matrix's singular value, representing the energy contained in each mode. ΣV^T represents the temporal coefficient of the mode.

The energy proportion E of the first N_{POD}-order reduced modes is given by:

$$E(N_{POD}) = \frac{\sum_{k=1}^{N_{POD}}\lambda_k}{\sum_{k=1}^{N}\lambda_k} \tag{14}$$

where λ_k is the value of each element in Σ.

Therefore, the truncation error of this method is optional. The more

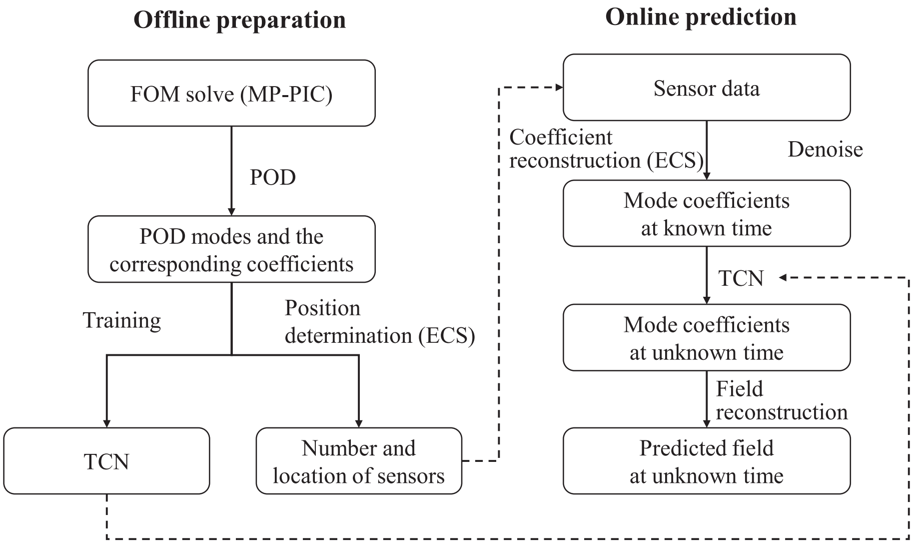

Fig. 1. Structure of the ECS-TCN-ROM model.

the number of POD modes selected, the more accurate the flow field composed of modes. The FOM field can be approximated as:

$$W(x,t) \approx W_0(x) + \sum_{k=1}^{N_{POD}} \alpha_k(t) \cdot \Phi_k(x) \tag{15}$$

where $W_0(x)$ is the time mean value of the target variable. $\alpha_k(t)$ is a coefficient that varies with time in transient simulations. $\Phi_k(x)$ is the orthogonal mode.

2.2.2. Enhanced compressed sensing

As shown in Fig. 1, ECS can be performed based on the obtained POD modes, which are used for both measurement point position determination and the compressed reconstruction of mode coefficients. Before determining the measurement point positions, it is necessary to clarify the compressed reconstruction method of the mode coefficients. The dominant spatial modes from POD are used to establish a mapping relationship between the measurements and mode coefficients, which can be mathematically expressed as:

$$Y = BX = B\Phi\alpha = \Theta\alpha \tag{16}$$

where the measurement data $Y \in \mathbb{R}^p$. p represents the number of measurement points. B represents the measurement point position (made entirely of 0 and 1). X stands for the FOM data. Θ is the transformation matrix and α is the mode coefficient matrix. When the number of measurement points equals the selected mode rank, Eq. (16) becomes a well-posed equation, and the mode coefficients can be directly solved from this equation. When the number of measurement points exceeds the selected mode rank, the mode coefficients corresponding to the number of measurement points can be reconstructed. Since the mode coefficients reconstructed by compressed sensing exceed the required number of modes, only a subset of these coefficients needs to be selected to construct the ROM. When the number of measurement points is less than the selected mode rank, Eq. (16) becomes an underdetermined system, leading to non-unique solutions. The minimum L2 norm solution for α needs to be determined. In summary, the equations for solving the mode coefficients are as follows, depending on whether the number of measurement points is not less than or less than the selected mode rank:

$$\alpha_0 = \Theta^{-1} Y \tag{17.1}$$

$$\alpha_0 = \Theta^T \left(\Theta\Theta^T\right)^{-1} Y \tag{17.2}$$

Based on the aforementioned compressed reconstruction method, the DEIM method is used to determine measurement point positions in this study. First, the position of the first measurement point, p_1, is identified. The position of the first measurement point is chosen as the position corresponding to the maximum absolute value of the first-order mode, i.e., it satisfies:

$$\Phi_1(p_1) = max\{\Phi_1^{abs}\} \tag{18}$$

Next, the position of the second and subsequent measurement sensors, p_j, is determined. Given that j-1 measurement points have already been acquired, the projection matrix ρ_{j-1} is defined as $\rho_{j-1} = \Psi(B^T\Psi)^{-1}B^T$. The position of the j-th measurement point, p_j, can be obtained from the judgment matrix χ_j as follows:

$$\chi_j\left(p_j\right) = max\{\chi_j^{abs}\} \tag{19}$$

$$\chi_j = \Phi_j - \rho_{j-1}\Phi_j = \Phi_j - \Psi\left(B^T\Psi\right)^{-1}B^T\Phi_j \tag{20}$$

where B is the measurement point position matrix(entirely composed of 0 and 1). Ψ is the mode matrix and $\Psi = \left[\Phi_1, \Phi_2, \cdots, \Phi_{j-1}\right]$.

Another method for determining measurement point placement is the QR-pivoting. The number of measurement points is no longer constrained by the rank of the POD modes. In this method, to optimize the compressed reconstruction effect in Eq. (17.2), it is necessary to maximize the determinant of $\Theta\Theta^T$ by selecting the measurement point position so that it is easier to invert, which is mathematically equivalent to maximizing the determinant of Θ. The determinant of Θ satisfies:

$$det(\Theta) = det\left(\Theta^T\right) = det\left(\Phi^T B^T\right) \tag{21}$$

Therefore, the mode matrix Φ^T is subjected to QR-pivoting to obtain:

$$\Phi^T P = QR \tag{22}$$

where the mode matrix Φ^T satisfies $\Phi^T \in \mathbb{R}^{N\times M}$, the column permutation matrix P satisfies $P \in \mathbb{R}^{M\times M}$, the unitary matrix Q satisfies $Q \in \mathbb{R}^{N\times N}$, and the upper triangular matrix R satisfies $R \in \mathbb{R}^{N\times M}$. The column permutation matrix permutes the column vectors of the matrix Φ^T so that the diagonal of the upper triangular matrix R is in decreasing order, further maximizing the absolute value of the determinant of Φ^T and optimizing the result of matrix inversion. Let the measurement point position matrix B be the first several rows of the permutation matrix P^T (the number of rows depends on the number of measurement points), and the optimal positions of the measurement points can be obtained.

However, the mode coefficients obtained by sparse measurements often have high-frequency noise fluctuations at the temporal level, which greatly reduce the accuracy of the flow field reconstructed by the ROM. Savitzky-Golay (S-G) filter (Savitzky and Golay, 1964) is combined to realize enhanced compressed sensing (ECS), further improving the reconstruction accuracy of the enhanced compressed sensing-reduced order model (ECS-ROM). In ECS, the mode coefficients are filtered:

$$\alpha = f_{sg}(\alpha_0) \tag{23}$$

2.2.3. Time coefficient prediction

In this study, the time prediction method is based on the previous literature (Li et al., 2024). TCN is a kind of convolutional neural networks (CNN) and is different from traditional image classification tasks. It has been demonstrated to exhibit excellent performance in time series prediction (Bai et al., 2018). Compared with long short-term memory neural networks (LSTM), TCN has better parallel computing capabilities and local perception capabilities, which can accelerate training and reasoning speed. A residual connection (Bai et al., 2018) is applied to the TCN, which helps prevent the network from converging to a local optimum. The structure of the TCN is shown in Fig. 2. The receptive field can be calculated using the following formula:

$$R_{field} = 2 \times (K-1) \times \sum_z D_z + 1 \tag{24}$$

where 2 represents that there are two convolution layers in a single residual block. K is the kernel size and D is a vector containing the dilations. In this study, $K = 2$ and $D = [1,2,4,8]$.

As for the realization and the parameters of TCN, the mode coefficients from 2 s to 10 s are selected as the training set and the mode coefficients from 10 s to 20 s are chosen as the test set. The learning rate of the TCN is 0.001 and the dropout value is 0.2. After normalizing the mode coefficients of different orders, the differences between mode orders can be disregarded, facilitating the training of a unified mode coefficient prediction neural network without the need to train separate networks for each mode order. Building on the TCN mentioned above, this approach allows the mode order differences to be ignored during inference, significantly enhancing inference speed. Based on the trained TCN, the mode time coefficient α^{output} of the flow field variable is predicted as follows:

$$\alpha^{output} = f_{TCN}\left(\alpha^{input}\right) \tag{25}$$

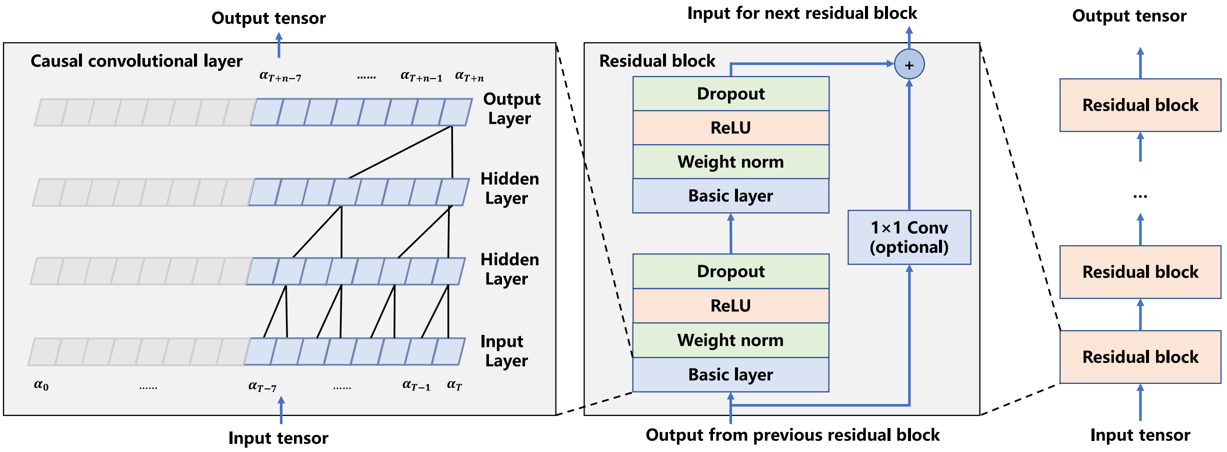

Fig. 2. Temporal convolution neural network structure.

2.2.4. *Online flow field reconstruction*

Based on the aforementioned POD, ECS, and TCN, a mapping relationship is established between the sparse measurements at the current time, the mode coefficients at the current time, the mode coefficients at the future time, and the flow field at the future time. The flow field is reconstructed in combination the existing POD mode Φ_k with the predicted POD coefficient α_k^n, as shown in Fig. 3. The reconstruction process is obtained by:

$$\widehat{W}(x,n) = W_0(x) + \sum_{k=1}^{N_{POD}} \alpha_k^n \cdot \Phi_k(x) \tag{26}$$

3. Numerical settings

3.1. *Geometry configuration and simulation setup*

The model mentioned above is used to implement the full-loop modeling of an industrial CFB boiler. This section introduces the geometry configuration and simulation setup. Fig. 4 shows the schematic diagram of the CFB. The CFB boiler system includes a chamber, cyclone separator, and U-type return feeder. The parameters used for numerical simulation are listed in Table 2. The diameters of the biomass particles and coal particles are set to 2 mm and 1 mm, with densities of 585 kg/m^3 and 1375 kg/m^3, respectively. The fuel proximate analysis is listed in Table S2 of the Supporting Information. The walls are all designed with no-slip and constant temperature boundary conditions. The physical time for FOM is 20 s. The time step is set to 0.001 s from 0 s to 2 s, and the time step is set to 0.0001 s from 2 s to 20 s. The snapshot time interval is 0.01 s, resulting in a total of 2000 snapshots. However, since the chemical reaction did not commence during the first 2 s, the actual number of snapshots used is 1800. As for the time series process, the first 1000 snapshots are used to train the TCN, and the last 800 snapshots are used to verify the accuracy of the TCN.

3.2. *Model validation of FOM*

Before applying the model to simulate real multi-physics processes, systematic validation is required. It is well known that fluid dynamics are highly correlated with heat and mass transfer in fluidized bed systems. Therefore, this section validates the FOM through experimental measurements of gas–solid thermophysical properties in a fluidized bed system, demonstrating its capability to reasonably capture the complex flow dynamics and heat and mass transfer processes within a CFB.

3.2.1. *Validation 1: 0.5MW$_{th}$ pilot-scale CFB*

The MP-PIC method is validated for co-combustion of refuse derived fuel (RDF) and coal in a 0.5 MW$_{th}$ pilot-scale CFB installed at Zhejiang University (Bai et al., 2012). The test rig has a furnace height of 11.2 m. The primary-to-secondary air ratio is maintained at 7:3, and the total mass flow rate of coal and RDF is 0.1736 kg/s. The density of coal particles is set to 1200 kg/m^3, while the density of RDF particles is set to 590 kg/m^3. Detailed settings can be found in our previous publication (Kong et al., 2020). As shown in Fig. 5, the time-averaged concentration of the main pollutants at the outlet of the cyclone separator is consistent with the experimental data. The temperature distribution within the furnace agrees well with the experiment, with a relative error of less than 8 %.

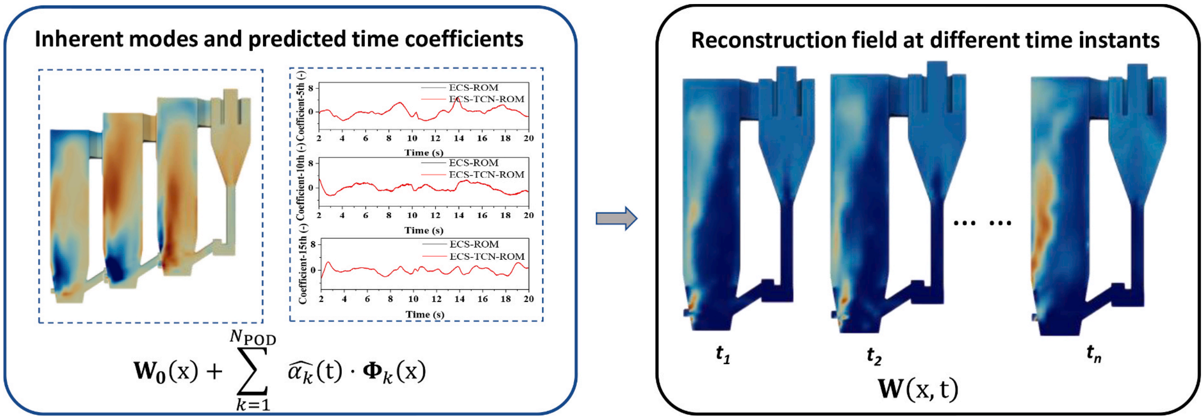

Fig. 3. Illustration of field reconstruction of the CFB.

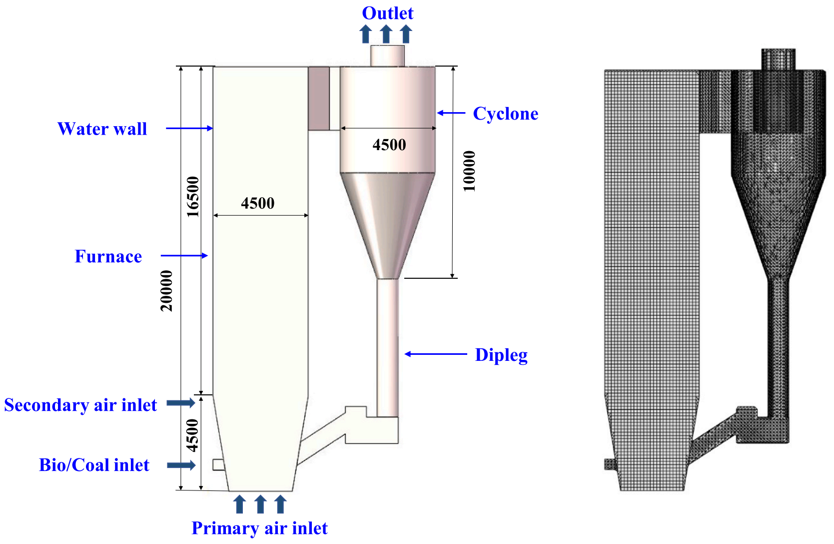

(a) (b)

Fig. 4. The geometry of the CFB. (a) geometric configuration; (b) computational grids.

Table 2
Parameters used for MP-PIC simulation.

Parameter	Gas flow rate	Solid flow rate
Primary air inlet (m/s)	5	–
Secondary air inlet (kg/s)	2.25	–
Loop-seal inlet (left) (m/s)	1	–
Loop-seal inlet (right) (m/s)	0.3	–
Biomass feed inlet (kg/s)	0.32255	1.736
Coal feed inlet (kg/s)	0.32255	0.306
Cyclone outlet	Atmosphere pressure	
Excess air ratio	1.3	–
Air temperature	473 K	–
Fuel temperature	–	473 K
water wall temperature	698 K	–

3.2.2. *Validation 2: 300MW$_{th}$ industrial-scale CFB*

The MP-PIC model is validated for gas–solid flow in a 300 MW$_{th}$ industrial-scale CFB boiler installed in Guangdong Province, China. The furnace height is 39.7 m, with primary and secondary air flow rates set at 474100 m^3/h and 333200 m^3/h, respectively. The densities of coal particles and bed material particles are set to 1300 kg/m^3 and 2600 kg/m^3, respectively. Detailed settings can be found in (Kong et al., 2023). The temperature field within the circulating fluidized bed reactor effectively reflects the heat transfer, mass transfer, and thermochemical characteristics within the furnace. By comparing the time-averaged temperature at a specific horizontal line in the current simulation with experimental data as shown in Fig. 6, it is found that the relative error between the predicted and experimental values is less than 4 %, and the temperature distribution profile is successfully captured, validating the reliability of the MP-PIC method. The authors have previously used the MP-PIC method for numerical simulations of biomass gasification (Wang et al., 2018), coal combustion and staged conversion (Kong et al., 2023; Ge et al., 2024), and co-combustion of coal with waste-derived fuels (Kong et al., 2020), demonstrating that the method provides sufficient precision in handling dense gas–solid reacting flows. Therefore, the MP-PIC model proposed in this study can provide a high-precision dataset for the ROM.

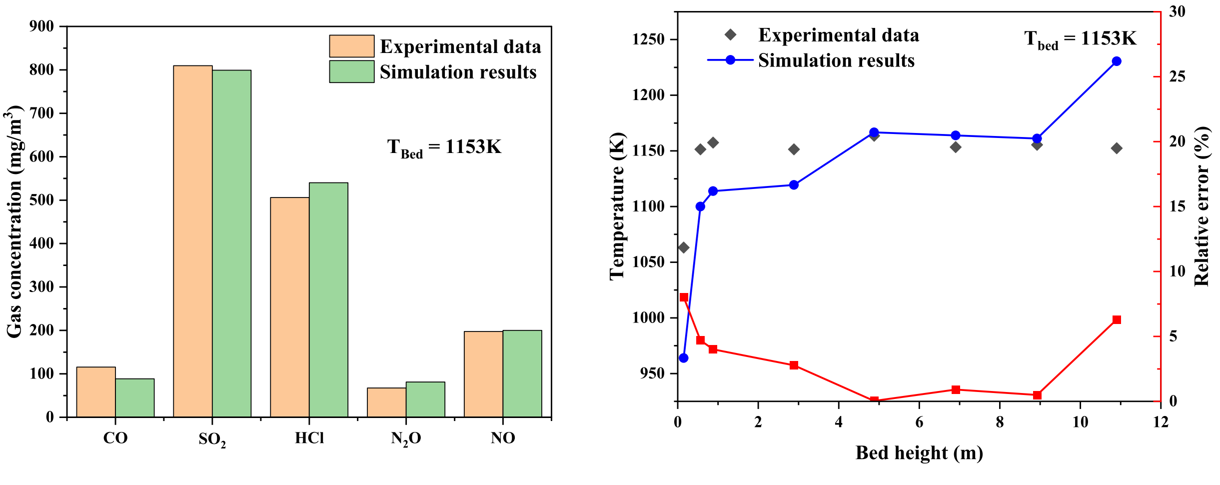

(a) (b)

Fig. 5. Comparisons between the simulation results and experimental data (Bai et al., 2012). (a) gas distribution; (b) temperature distribution.

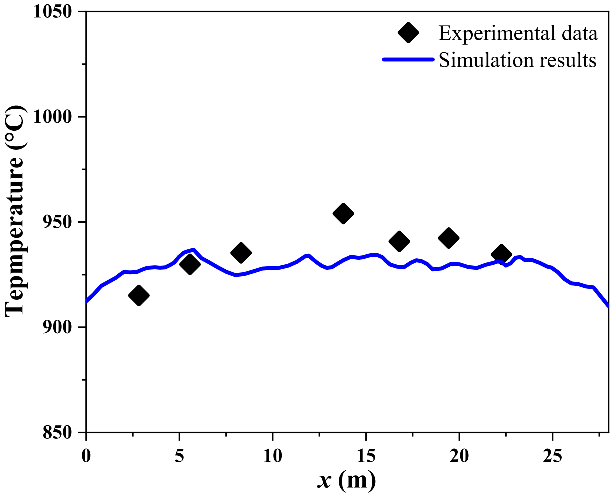

Fig. 6. Comparison of the horizontal temperature distribution between the simulation results and experimental data.

4. Results and discussion

This section validates the ECS-TCN-ROM in a CFB. The first part of this section covers the offline preparation phase of the ECS-TCN-ROM, including POD, ECS, and TCN training. POD is performed on the variables of interest in CFB, such as the mass fraction of CO_2. Subsequently, ECS is performed based on the decomposed modes. The mode coefficients are reconstructed through the sparse measurements in the physical space. After obtaining the mode coefficients at the current time through ECS, TCN is trained to predict the mode coefficients at future times, enabling early warning. The second part of this section describes the online prediction process of the ECS-TCN-ROM. Based on the developed model, online predictions are made for CO_2 mass fraction, temperature, and particle volume fraction, followed by an assessment of the prediction errors. The predicted mode coefficients and the modes obtained by POD are linearly combined to reconstruct the full flow field.

4.1. Offline preparation

4.1.1. POD analysis

Dense gas–solid reaction flow contains variables such as particle volume fraction, temperature, and species mass fraction. Only the POD analysis of the CO_2 mass fraction is shown in this section. Fig. 7 illustrates the variation in mode energy. It can be found that the mode energy distribution of CO_2 is not concentrated. Due to the strong nonlinear characteristics of multi-physics coupling in dense gas–solid flow, the distribution characteristics of chemical species are not easy to capture. When the number of modes is 240 and 479, it can contain 80 % and 90 % of the characteristics of the flow field, respectively. As shown in Fig. 8, the first 10 modes of the CO_2 mass fraction are presented, which reflect the main distribution characteristics of the CO_2 mass fraction. In the first and second modes, CO_2 exhibits a low concentration at the fuel inlet, representing the primary characteristic of CO_2 distribution. The differences in CO_2 mass fraction across the various modes are mainly concentrated at the fuel inlet and the wall surfaces on the inlet side.

4.1.2. Enhanced compressed sensing

After POD decomposes the FOM snapshots, the spatial modes can be used to identify the optimal sparse measurement point positions. Following ECS, a mapping relationship between measurements and mode coefficients can be established, enabling the coupling of physical and digital spaces. In the following, RMSE is used as the basis for the reconstruction accuracy of CS and ECS. The calculation method of RMSE is:

$$\text{RMSE} = \sqrt{\frac{1}{n}\sum_{i=1}^{n}(y_i - \widehat{y}_i)^2} \tag{27}$$

where, y_i is the actual value , $\widehat{y}_i$ is the predicted value, and n is the number of data. There are complex multiphase and multi-physics coupling processes in a CFB, and traditional CS may not be feasible when the number of measurement points is too small. As the number of measurement points increases, the accuracy of CS gradually improves. However, in industrial applications, using an excessive number of measurement points is often impractical, resulting in inevitable noise fluctuations. To reduce noise in the mode coefficients, an ECS-ROM is developed, which couples a CS-ROM with an adaptive Savitzky-Golay (S-G) filter. The S-G filter denoises the noise in the mode coefficients through a sliding window. However, high-precision denoising across all frequencies of the mode coefficients is not achievable due to the sliding window nature of the filters. ECS-ROM narrows the sliding window as the dominant frequency of the mode coefficients increases, enabling high-precision denoising for mode coefficients with different dominant frequencies. After developing the adaptive denoising algorithm, the

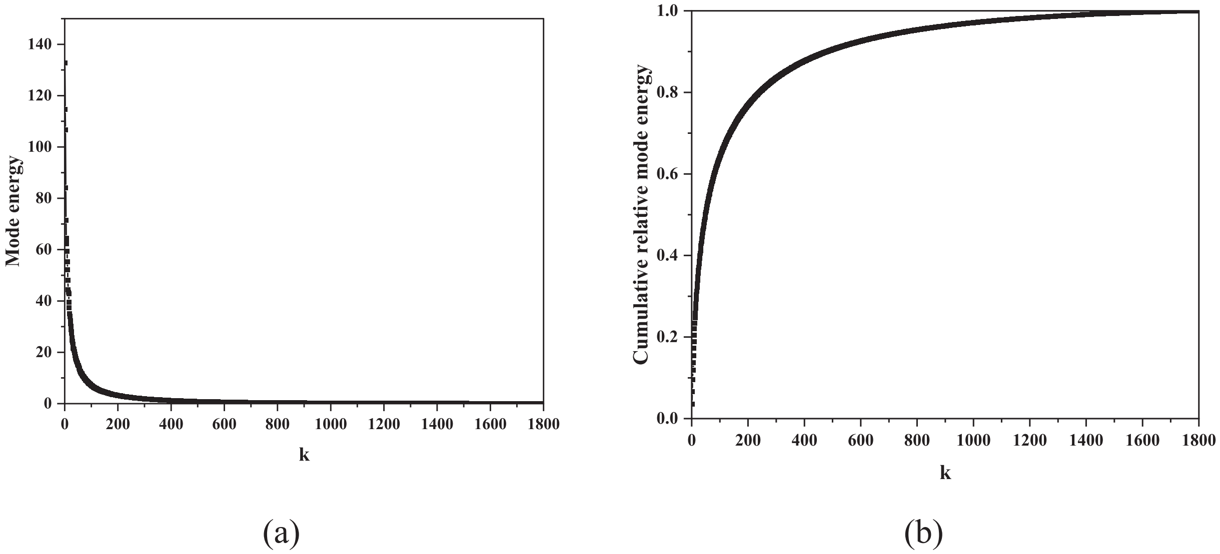

Fig. 7. CO_2 mass fraction distribution of the first 10 orders of POD modes. (a) mode energy; (b) mode cumulative relative mode energy.

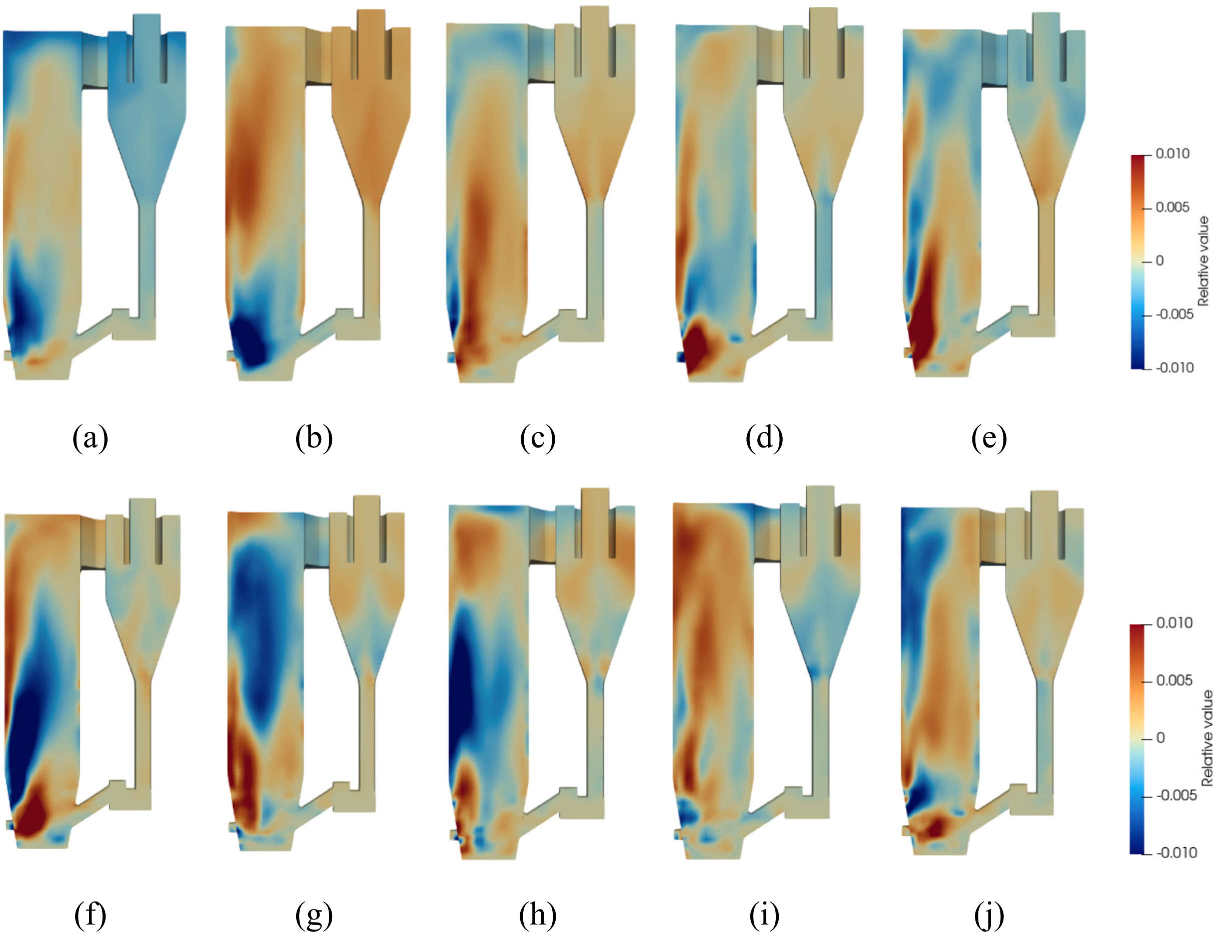

(a) (b) (c) (d) (e)

(f) (g) (h) (i) (j)

Fig. 8. The distribution of CO_2 mass fraction at the first 10 orders of POD modes. (a) 1st mode; (b) 2nd mode; (c) 3rd mode; (d) 4th mode; (e) 5th mode; (f) 6th mode; (g) 7th mode; (h) 8th mode; (i) 9th mode.

ECS-ROM coupled with the S-G filter provides higher accuracy, as shown in Fig. 9. Among them, the number of measurement points and the number of modes used in Fig. 9(a) and Fig. 9(b) are both 100. The number of modes used in Fig. 9 (c) is 100.

The two measurement point selection methods, DEIM and QR-pivoting, are compared. The comparison between the two is shown in Fig. 10. The number of measurement points and modes used is consistent with that in Fig. 9. The reconstruction accuracy of QR-pivoting is significantly lower compared to the DEIM method. Except when the number of measurement points is 50, where the RMSE of mode coefficients reconstructed by DEIM reaches 0.56, all other RMSEs are below 0.17. In contrast, the RMSE of mode coefficients reconstructed by QR-pivoting ranges from 0.75 to 1.52. Therefore, DEIM is adopted for measurement point position determination in the subsequent analysis.

The number of measurement points can be chosen based on the desired accuracy for the specific industrial process. A parametric analysis is conducted to determine the optimal number of measurement points. As shown in Fig. 11 (a), (b), and (c), an analysis of the RMSE for

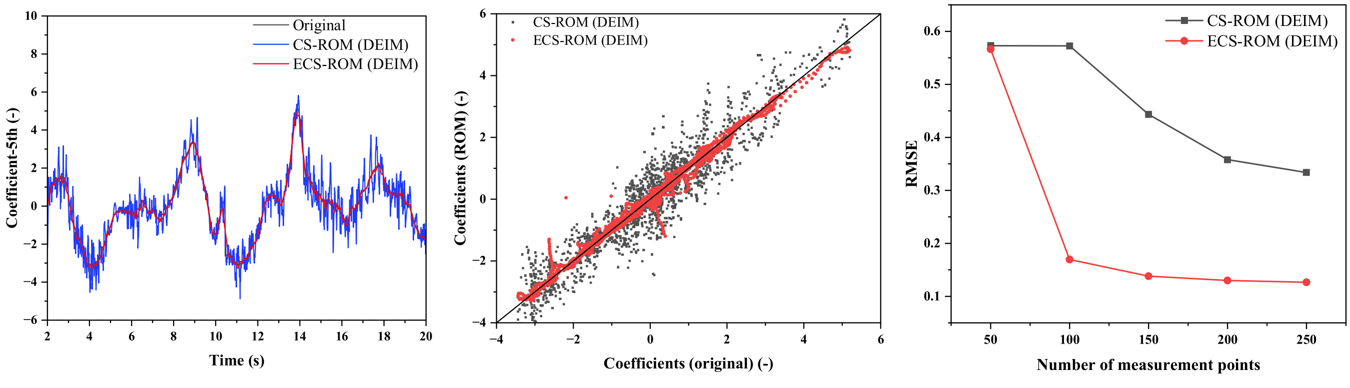

(a) (b) (c)

Fig. 9. The comparison of the CS-ROM (DEIM) and ECS-ROM (DEIM). (a)the 5th mode coefficient evolution of CO_2 mass fraction; (b) the 5th mode coefficient parity plot between the ROM and the original coefficient; (c) the ROM RMSE for different measurement points.

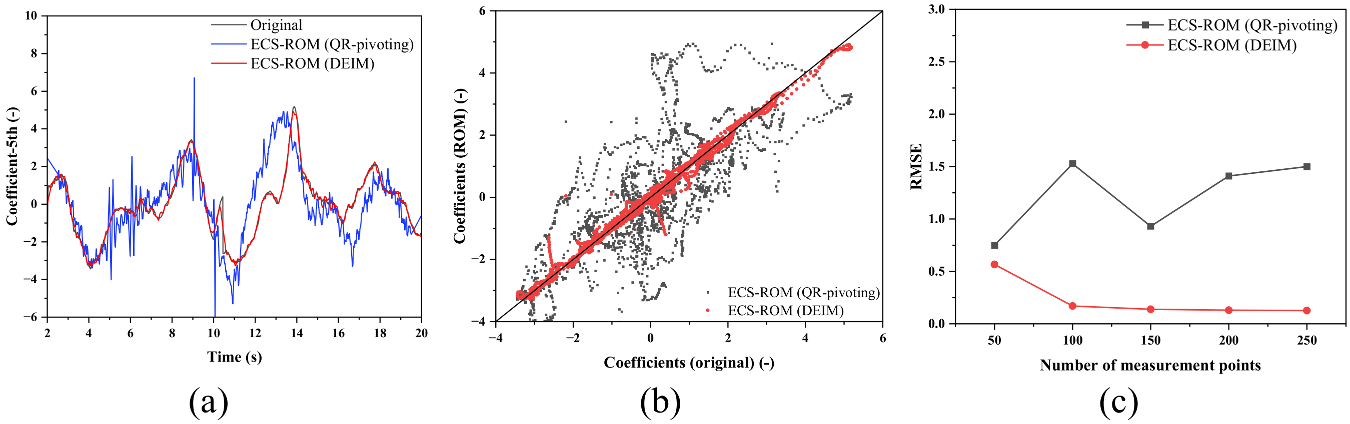

Fig. 10. The comparison of the ECS-ROM (QR-pivoting) and ECS-ROM (DEIM). (a)the 5th mode coefficient evolution of CO_2 mass fraction; (b) the 5th mode coefficient parity plot between the ROM and the original coefficient; (c) the ROM RMSE for different measurement points.

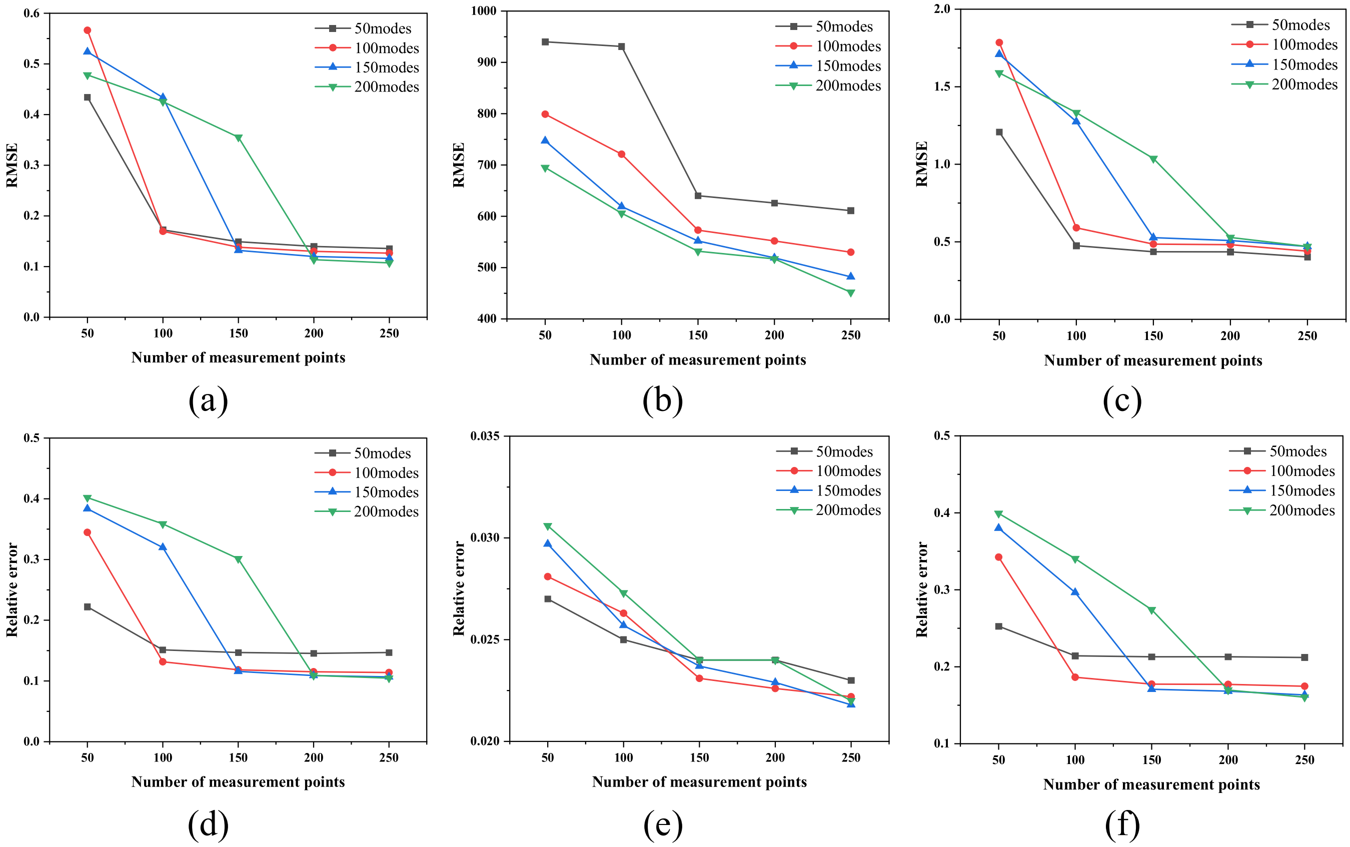

Fig. 11. The RMSE and relative error for different mode numbers and measurement point numbers. (a) RMSE of CO_2 mass fraction; (b) relative error of CO_2 mass fraction; (c) RMSE of temperature; (d) relative error of temperature; (e) RMSE of particle volume fraction; (f) relative error of particle volume fraction.

CO_2 mass fraction, temperature, and particulate volume fraction reveals that the number of measurement points and the number of selected reconstruction modes are correlated. When the number of measurement points meets or exceeds the required modes, the ECS-ROM achieves a lower RMSE. Otherwise, the RMSE increases significantly. With the number of modes held constant, the RMSE of the ECS-ROM decreases as the number of measurement points increases. However, with the number of measurement points held constant (considering the correlation between measurement point number and mode number, this analysis assumes the number of measurement points is greater than the number of modes), the RMSE does not necessarily decrease with the increase in the number of modes. This is because the prediction errors of higher-order mode coefficients, which have higher frequencies and more complex fluctuations, may increase, resulting in a higher overall RMSE.

The accuracy of the ECS-ROM is influenced by both the ECS reconstruction accuracy (RMSE) and the number of selected reconstruction modes. Therefore, relying solely on the ECS reconstruction accuracy (RMSE) of the ECS-ROM to determine the number of measurement points is insufficient. Based on this, a further comparison of the relative errors is conducted, as shown in Fig. 11 (d), (e), and (f). It is observed that the variation in relative error with the number of measurement points follows a similar trend to that of RMSE as a function of the number of measurement points. However, in certain specific cases, such as for the particle volume fraction, when the “measurement point-mode” combinations are “150–100” and “150–150”, the RMSE for the “150–100” is lower, while the relative error for the “150–150” is smaller. This is because, with other conditions constant, the ROM with 150 modes inherently offers better accuracy than the ROM with 100 modes. Therefore, despite a decrease in the prediction accuracy of the mode coefficients, the increased number of modes compensates for this effect, resulting in higher ROM accuracy. Taking the ECS-ROM of 100 modes for CO_2 mass fraction as an example, Fig. 12 illustrates the CO_2 mass fraction distribution for different numbers of measurement points. It can be observed that when the number of measurement points exceeds 100, many features in the furnace can be well reproduced. However, there is a significant discrepancy between the ECS-ROM and the FOM when the number of measurement points is reduced to 50. The distribution patterns of $CO_{2,}$ such as the low concentration zones in the furnace, cannot be captured. Considering both the economic feasibility and accuracy of measurement points, the ECS-ROMs for CO_2 mass fraction, temperature, and particulate volume fraction are constructed using “measurement point-mode” combinations of “100–100”, “150–100”, and “100–100”, respectively.

4.1.3. *Time coefficient prediction*

This section uses the coefficients obtained from the ECS-ROM as inputs and the mode coefficients at future time steps as outputs to train the TCN. The input time step number of TCN is 30. In the authors’ previous work (Li et al., 2024), it has been demonstrated that when the input and output time steps are consistent, both accuracy and efficiency can be effectively balanced. Therefore, the output time step number is kept consistent with the input time step number, which is 30. Due to space limitations, Fig. 13 presents only the time series predictions of the 5th, 10th, and 15th mode coefficients for CO_2 mass fraction, temperature, and particle volume fraction. TCN performs well for mode coefficients at different frequencies, maintaining exceptionally high accuracy when predicting the mode coefficients over the next 30 time steps, thus laying the foundation for the advanced control of digital twins.

4.2. *Online prediction*

After completing the offline preparation, including POD, ECS, and TCN, the ECS-TCN-ROM construction enters the online stage. First, the reconstruction errors for CO_2 mass fraction, temperature, and particle volume fraction are analyzed. Fig. 14 shows the error evolution for TCN-ROM and ECS-TCN-ROM. The error in (a) represents the snapshot average error corresponding to different numbers of modes. The reconstruction errors of both TCN-ROM and ECS-TCN-ROM gradually decrease as the number of modes increases. The error in (b) represents the transient error of the ECS-TCN-ROM and TCN-ROM over time. The reconstruction errors for TCN-ROM and ECS-TCN-ROM remain stable as time progresses. The ECS-TCN-ROM error is slightly larger than the TCN-ROM error since certain details are inevitably overlooked during the ECS, leading to increased error. Notably, compared to CO_2 mass fraction and particle volume fraction, the temperature ROM reconstruction error is smaller.

Fig. 15 illustrates the distribution of the CO_2 mass fraction predicted by TCN-ROM and ECS-TCN-ROM. The CO_2 mass fraction obtained from TCN-ROM has a small error compared to FOM and exhibits better accuracy performance. ECS-TCN-ROM can provide an approximate distribution of the CO_2 mass fraction, but it overlooks some details. The CO_2 mass fraction and particle volume fraction approach zero in certain regions. If relative error is used for calculation, the errors in those regions would be extremely large, which is not conducive to error distribution analysis. Therefore, in this paper, for consistency, absolute error analysis is applied to the CO_2 mass fraction, temperature, and particle volume fraction. The same phenomenon observed in the CO_2 mass fraction ROM is also evident in the temperature ROM and particle volume fraction ROM, as shown in Figs. 16 and 17.

Flow fields at different time points are selected for a more quantitative comparison. Five cross-sections at heights of 3 m, 6 m, 9 m, 12 m, and 15 m within the furnace are averaged to analyze the variation of variables at different elevations. The specific changes are shown in Fig. 18. The ECS-TCN-ROM effectively captures the characteristics of the flow field.

Furthermore, the inference time of ECS-TCN-ROM is compared. Once again, the output time steps of TCN are consistent with the input time steps. The ECS-TCN-ROM includes 3 steps: POD, enhanced compressed sensing, and prediction. Since both the POD and the determination of measurement point locations in ECS are carried out offline, they are not included in the online prediction time of the ECS-TCN-ROM. Table 3 presents the offline time consumption for POD and ECS (offline preparation), including the time required by ECS to determine the measurement point positions for both the required number of measurement points (100/150/100) and all 1800 measurement points. Table 4 shows the online time consumption of the FOM and ECS-TCN-ROM over 30 time snapshots (physical time is 0.3 s). The offline preparation run with a 16-core and the online prediction run with a single core (Intel(R) Core (TM) i5-14400 2.50 GHz). It is important to note that the ROM simulation time in this paper refers to a single variable. Since all variables are coupled and solved in FOM, the FOM simulation time refers to all variables. The reduction is defined as the ratio of FOM (MP-PIC) time to ECS-TCN-ROM time. Among these cases, the simulation efficiency of ECS-TCN-ROM increases by about 25,000 times. In summary, the ECS-TCN-ROM proposed in this paper takes the sparse measurement points

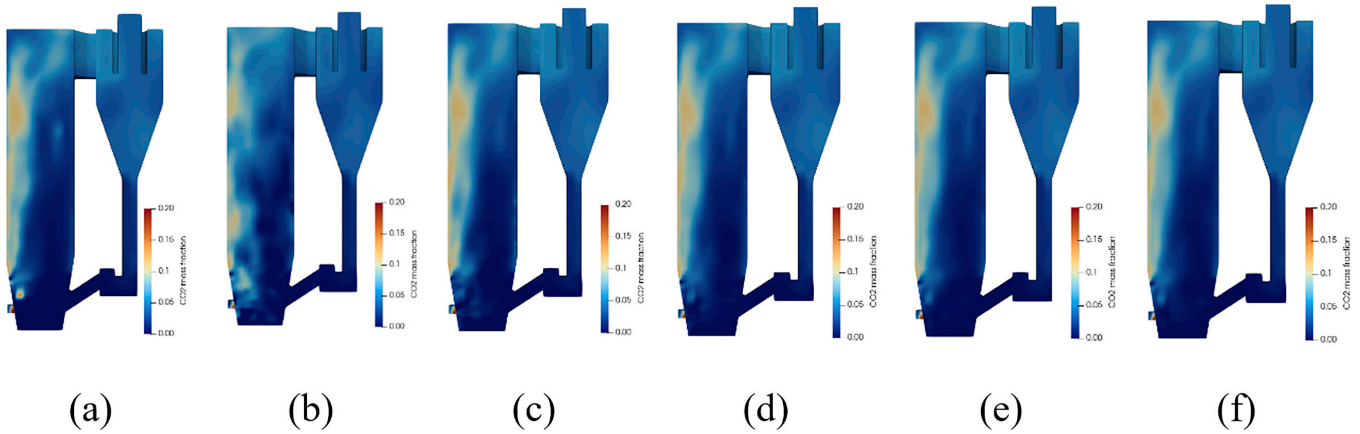

Fig. 12. CO_2 mass fraction predicted by POD-ROM. (a) FOM; (b) ECS-ROM-50 measurement points; (c) ECS-ROM-100 measurement points; (d) ECS-ROM-150 measurement points; (e) ECS-ROM-200 measurement points; (f) ECS-ROM-250 measurement points.

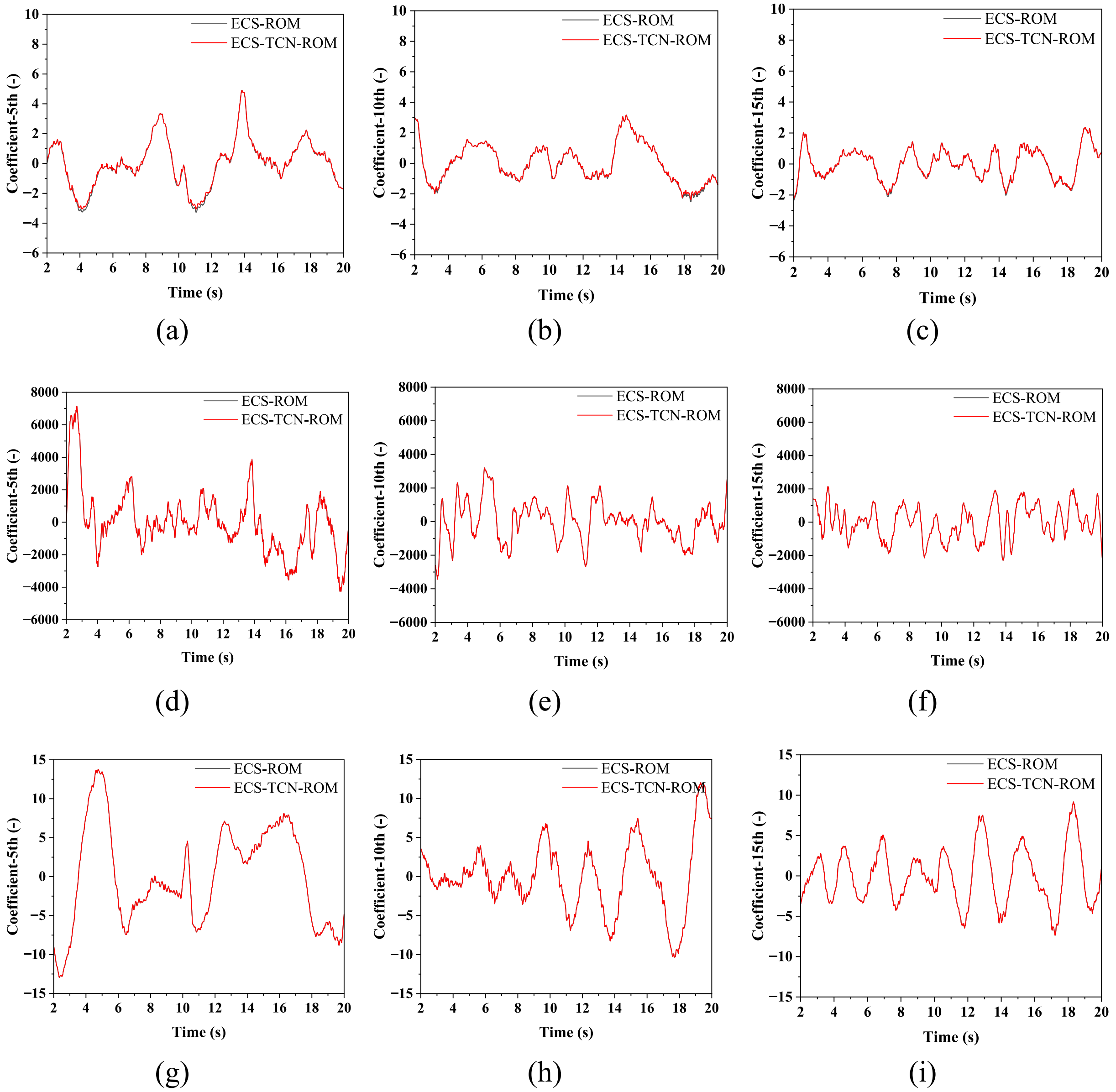

Fig. 13. The mode coefficients predicted by TCN. (a) 5th mode coefficient of CO_2 mass fraction; (b) 10th mode coefficient of CO_2 mass fraction; (c) 15th mode coefficient of CO_2 mass fraction; (d) 5th mode coefficient of temperature; (e) 10th mode coefficient of temperature; (f) 15th mode coefficient of temperature; (g) 5th mode coefficient of particle volume fraction; (h) 10th mode coefficient of particle volume fraction; (i) 15th mode coefficient of particle volume fraction.

in the physical space at the current time as input, uses mode decomposition and machine learning methods to obtain the full flow field at the future time, and realizes the virtual-real mapping effect of the digital twin.

5. Conclusions

This study proposes a novel ECS-TCN-ROM for dense gas–solid flow in a CFB. The POD, ECS, and time series prediction are deeply coupled in the ECS-TCN-ROM, which constructs a mapping relationship that takes sparse measurement points in the physical space at the current moment as input and full-field flow at the future moment as output. The conclusions are as follows:

1) Some key variables in the CFB, such as CO_2 mass fraction, are properly orthogonally decomposed. The main modes of CO_2 mass fraction reflect the main characteristics of the CO_2 mass fraction distribution.
2) The mode coefficients obtained through CS often exhibit noise fluctuations. The ECS-TCN-ROM, coupled with an adaptive denoising algorithm, achieves higher reconstruction accuracy with fewer measurement points.
3) Although the ECS-TCN-ROM incurs a larger error compared to the TCN-ROM, it further eliminates the idealized assumptions of the TCN-ROM, with the error remaining within industrially acceptable limits.
4) The ECS-TCN-ROM achieves a four-order-of-magnitude acceleration, laying the foundation for the realization of digital twins.

It is worth noting that this paper theoretically establishes a mapping relationship from sparse measurement points in physical space to the full flow field in digital space, although all data are based on CFD simulation results. For instance, the data of FOM is based on CFD, and ECS-TCN-ROM assumes the grid point data in the CFD simulation results as physical space input. In addition, in real-world CFBs, measurement sensors are typically placed on the walls at the furnace inlet and outlet.

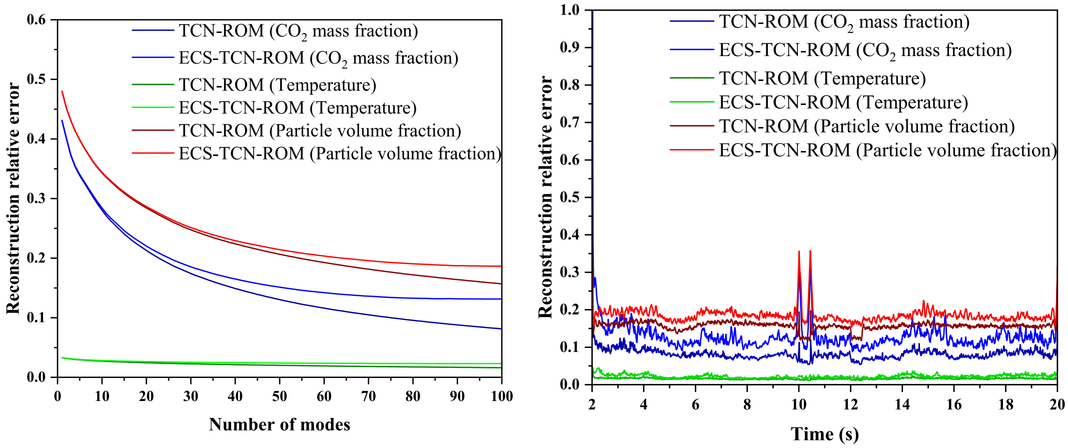

(a) (b)

Fig. 14. Error predicted by TCN-ROM and ECS-TCN-ROM. (a) error varying with the number of modes; (b) error varying with time.

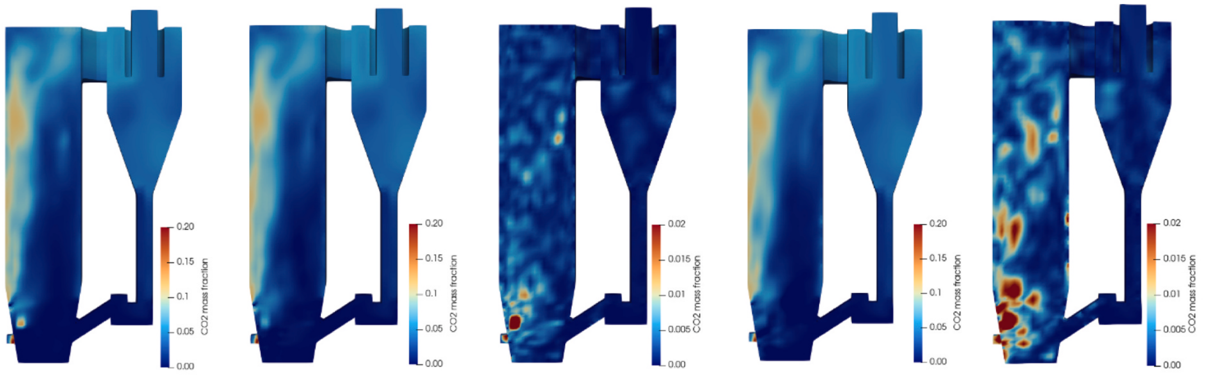

(a) (b) (c) (d) (e)

Fig. 15. CO_2 mass fraction. (a) FOM; (b) TCN-ROM; (c) absolute error of TCN-ROM; (d) ECS-TCN-ROM; (e) absolute error of ECS-TCN-ROM.

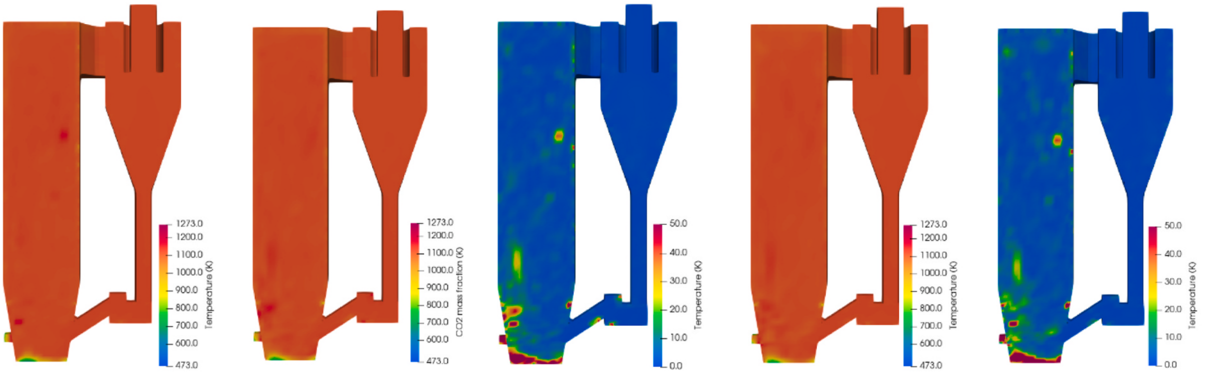

(a) (b) (c) (d) (e)

Fig. 16. Temperature. (a) FOM; (b) TCN-ROM; (c) absolute error of TCN-ROM; (d) ECS-TCN-ROM; (e) absolute error of ECS-TCN-ROM.

The number of measurement points is generally limited, and the measurements are often noisy. In future research, it is planned to replace the input in CS with the data from real physical space, while considering the aforementioned limitations, and then build a real virtual-real digital twin system. The method proposed in this paper provides a way to implement the digital twin of the actual industrial production process.

CRediT authorship contribution statement

Xiaofei Li: Writing – original draft, Visualization, Validation, Software, Methodology, Investigation, Formal analysis, Data curation. **Shuai Wang:** Writing – review & editing, Supervision, Project administration, Funding acquisition, Conceptualization. **Kun Luo:** Writing – review & editing, Supervision, Project administration, Funding acquisition, Conceptualization. **Jianren Fan:** Supervision, Project

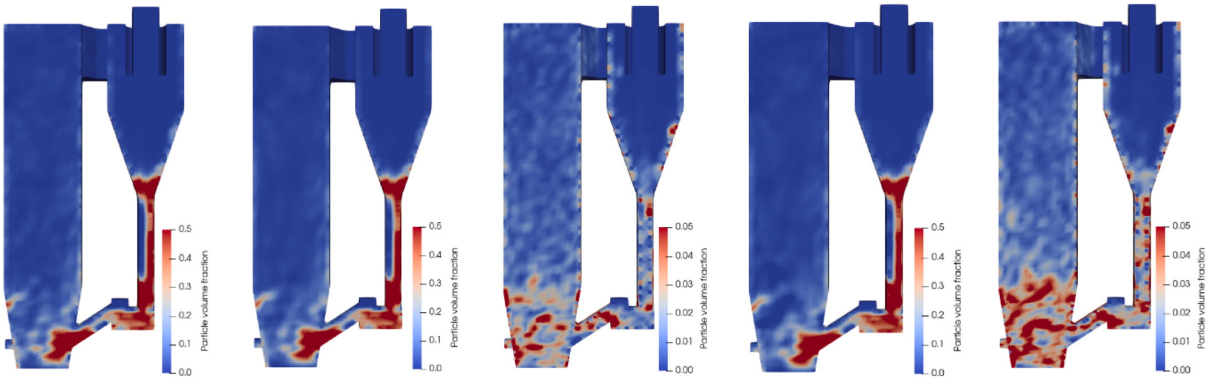

(a) (b) (c) (d) (e)

Fig. 17. Particle volume fraction. (a) FOM; (b) TCN-ROM; (c) absolute error of TCN-ROM; (d) ECS-TCN-ROM; (e) absolute error of ECS-TCN-ROM.

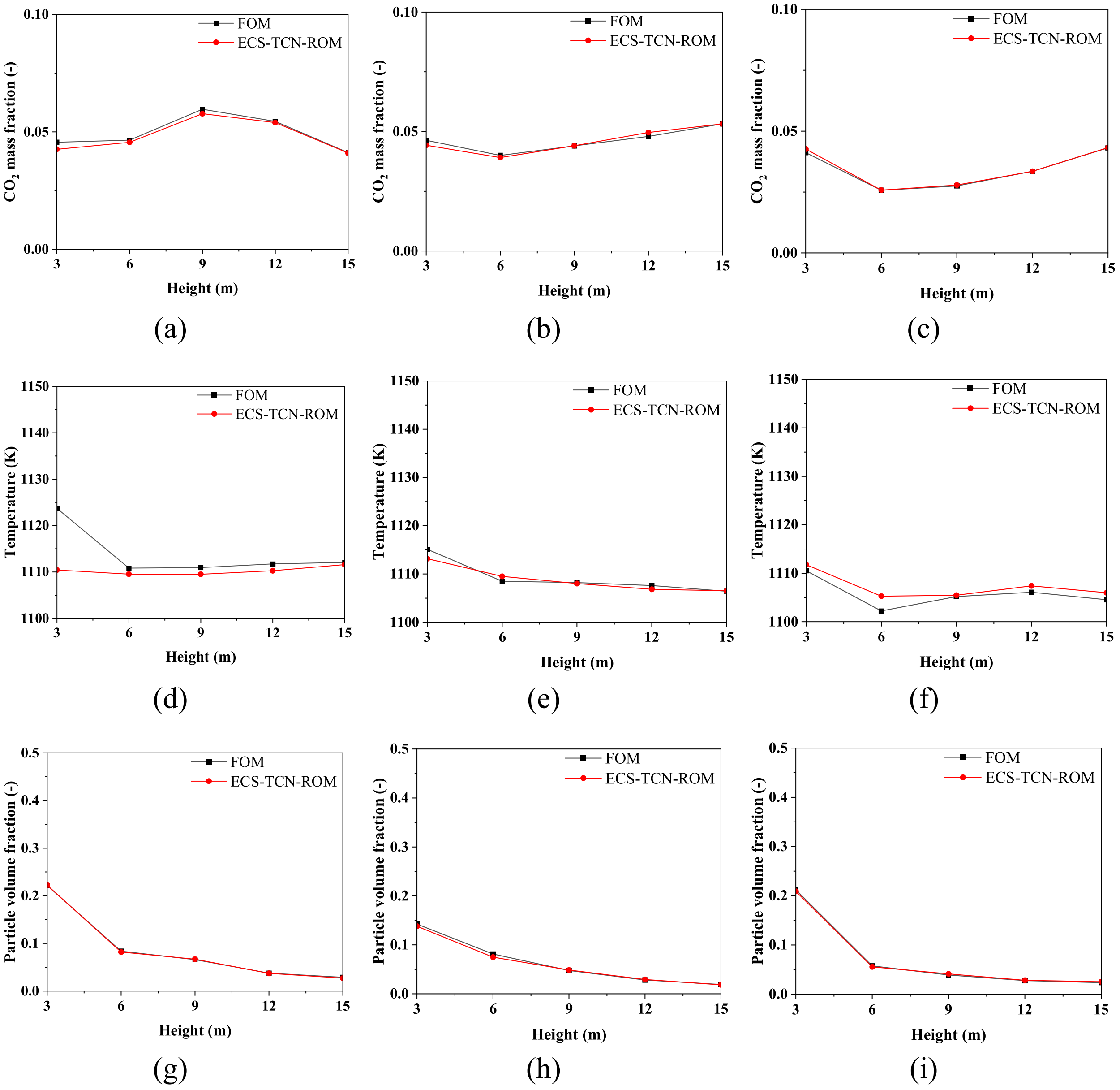

(a) (b) (c)

(d) (e) (f)

(g) (h) (i)

Fig. 18. Comparison between the FOM and the ECS-TCN-ROM at different cross-sections. (a)-(c): CO_2 mass fraction at 12.5 s, 15 s, 17.5 s; (d)-(f): temperature at 12.5 s, 15 s, and 17.5 s; (g)-(i): particle volume fraction at 12.5 s, 15 s, and 17.5 s.

Table 3
Offline time consumption of the POD and the ECS (preparatory phase).

Variable	POD [s]	ECS (offline preparation) [s]	
		Required number of measurement points	All 1800 measurement points
CO_2 mass fraction	22.31	4.28	5318
Temperature	22.61	10.27	5420
Particle voidage	21.73	4.34	5429

Table 4
Online time consumption of the FOM and ECS-TCN-ROM.

Variable	Model	CFD [s]	Prediction [s]	Reduction
CO_2 mass fraction	FOM	68	–	–
	ECS-TCN-ROM	–	0.0026	26,153
Temperature	FOM	68	–	–
	ECS-TCN-ROM	–	0.0028	24,285
Particle voidage	FOM	68	–	–
	ECS-TCN-ROM	–	0.0025	27,200

administration.

Declaration of competing interest

The authors declare that they have no known competing financial interests or personal relationships that could have appeared to influence the work reported in this paper.

Acknowledgements

We are grateful for the supports from National Natural Science Foundation of China (Grant No. 588020-X42405), National Key Research and Development Plan of China (Grant No. 2024YFB4105902), Key Research and Development Program of Zhejiang Province (Grant No. 2025C01047), Fundamental Research Funds for the Central Universities (Grant No. 226-2024-00138), Shanghai Pujiang Program (Grant No. 23PJ1412000), and Xplorer Prize.

Appendix A. Supplementary data

Supplementary data to this article can be found online at https://doi.org/10.1016/j.ces.2025.122003.

Data availability

Data will be made available on request.

References

Ansari, A.B., 2023. Reduced-order modeling of PEM fuel cell based on POD and PODI: an efficient approach toward combining highest accuracy with real-time performance. Int. J. Hydrogen Energy. S0360319923018311.

Aversano, G., Ferrarotti, M., Parente, A., 2021. Digital twin of a combustion furnace operating in flameless conditions: reduced-order model development from CFD simulations. Proc. Combust. Inst. 38, 5373–5381.

Bai S, Kolter JZ, Koltun V. 2018. An Empirical Evaluation of Generic Convolutional and Recurrent Networks for Sequence Modeling. arXiv.

Bai, J., Yu, C., Li, L., et al., 2012. Experimental investigation on co-firing of coal and refuse-derived fuel in a pilot-scale circulating fluidized bed combustor. Proc. CSEE 32, 36–41.

Barrault, M., Maday, Y., Nguyen, N.C., et al., 2004. An 'empirical interpolation' method: application to efficient reduced-basis discretization of partial differential equations. Comptes Rendus. Mathématique 339, 667–672.

Berkooz G, Holmes P, Lumley JL, 1993. The Proper Orthogonal Decomposition in the Analysis of Turbulent Flows.

Bright, I., Lin, G., Kutz, J.N., 2013. Compressive sensing based machine learning strategy for characterizing the flow around a cylinder with limited pressure measurements. Phys. Fluids 25, 127102.

Businger, P., Golub, G.H., 1965. Linear least squares solutions by householder transformations. Numer. Math. 7, 269–276.

Chen, H., Li, W., Bao, J., et al., 2025. A mPOD-based reduced-order modelling approach for fast gas-solid flow simulations. Chem. Eng. Sci. 121155.

Chen, H., Li, W., Bao, J., et al., 2025. A mPOD-based reduced-order modelling approach for fast gas-solid flow simulations. Chem. Eng. Sci. 306, 121155.

Cheng, S., Prentice, I.C., Huang, Y., et al., 2022. Data-driven surrogate model with latent data assimilation: application to wildfire forecasting. J. Comput. Phys. 464, 111302.

Fang, J., Cu, W., Liu, H., et al., 2024. Data driven reduced modeling for fluidized bed with immersed tubes based on PCA and bi-LSTM neural networks. Particuology 91, 1–18.

Ge, Y., Yu, J., Lin, J., et al., 2024. Multiphase flow and reactor optimization of a 1MWth pilot-scale circulating fluidized bed for coal staged conversion. Chem. Eng. J. 484, 149524.

Gomes D, Espírito Santo A, Páscoa JC. 2024. Theoretical Framework and Use of CNN Reconstruction With Optimal Sparse Sensor Placement in a Flow Field[C]//Volume 8: Fluids Engineering. Portland, Oregon, USA: American Society of Mechanical Engineers. V008T10A007.

Hajisharifi, A., Romanò, F., Girfoglio, M., et al., 2023. A non-intrusive data-driven reduced order model for parametrized CFD-DEM numerical simulations. J. Comput. Phys. 491, 112355.

Hajisharifi, A., Halder, R., Girfoglio, M., et al., 2024. An LSTM-enhanced surrogate model to simulate the dynamics of particle-laden fluid systems. Comput. Fluids 280, 106361.

Jayaraman, B., Mamun, S.M.A.A., 2020. On data-driven Sparse sensing and Linear estimation of fluid flows. Sensors 20, 3752.

Jiang, G., Kang, M., Cai, Z., et al., 2022. Online reconstruction of 3D temperature field fused with POD-based reduced order approach and sparse sensor data. Int. J. Therm. Sci. 175, 107489.

Kong, D., Wang, S., Zhou, M., et al., 2020. Three-dimensional full-loop numerical simulation of co-combustion of coal and refuse derived fuel in a pilot-scale circulating fluidized bed boiler. Chem. Eng. Sci. 220, 115612.

Kong, D., Wang, S., Yu, J., et al., 2023. Investigation of non-uniform characteristics in a 300 MWth circulating fluidized bed with different coal feeding modes. Adv. Powder Technol. 34, 104036.

Ku, X., Li, T., Løvås, T., 2015. CFD–DEM simulation of biomass gasification with steam in a fluidized bed reactor. Chem. Eng. Sci. 122, 270–283.

Li, S., Duan, G., Sakai, M., 2022. Development of a reduced-order model for large-scale Eulerian–Lagrangian simulations. Adv. Powder Technol. 33, 103632.

Li, S., Duan, G., Sakai, M., 2024. On reduced-order modeling of gas–solid flows using deep learning. Phys. Fluids 36, 033340.

Li, X., Wang, S., Kong, D., et al., 2024. Data-driven reduced-order model for bubbling fluidized beds. Ind. Eng. Chem. Res. 63, 1634–1648.

Li, X., Xu, Q., Wang, S., et al., 2024. A novel data-driven reduced-order model for the fast prediction of gas-solid heat transfer in fluidized beds. Appl. Therm. Eng. 253, 123670.

Loiseau, J.-C., Noack, B.R., Brunton, S.L., 2018. Sparse reduced-order modelling: sensor-based dynamics to full-state estimation. J. Fluid Mech. 844, 459–490.

Luo, Z., Wang, L., Xu, J., et al., 2023. Flow reconstruction from sparse sensors based on reduced-order autoencoder state estimation. Phys. Fluids 35, 075127.

Menges, D., Rasheed, A., Martens, H., et al., 2024. Real-time predictive condition monitoring using Multivariate data. IEEE Trans. Image Process. 33, 5703–5714.

Nair, N.J., Goza, A., 2020. Leveraging reduced-order models for state estimation using deep learning. J. Fluid Mech. 897, R1.

Procacci, A., Amaduzzi, R., Coussement, A., et al., 2022. Adaptive digital twins of combustion systems using sparse sensing strategies. Proc. Combust. Inst., S1540748922000712

Procacci, A., Amaduzzi, R., Coussement, A., et al., 2024. Computed tomography of chemiluminescence using a data-driven sparse sensing framework. Appl. Therm. Eng. 255, 123918.

Rao, P.P., 2024. Inverse parameter estimation using compressed sensing and POD-RBF reduced order models. Comput. Methods Appl. Mech. Eng. 422, 116820.

Sargsyan, S., Brunton, S.L., Kutz, J.N., 2015. Nonlinear model reduction for dynamical systems using sparse sensor locations from learned libraries. Phys. Rev. E 92, 033304.

Savitzky, A., Golay, M.J.E., 1964. Smoothing and differentiation of data by simplified least squares procedures. Anal. Chem. 36, 1627–1639.

Wang, S., Luo, K., Hu, C., et al., 2018. Impact of operating parameters on biomass gasification in a fluidized bed reactor: an Eulerian-lagrangian approach. Powder Technol. 333, 304–316.

Wang, S., Luo, K., Fan, J., 2020. CFD-DEM coupled with thermochemical sub-models for biomass gasification: validation and sensitivity analysis. Chem. Eng. Sci. 217, 115550.

Xie, J., Zhong, W., Shao, Y., et al., 2017. Simulation of combustion of municipal solid waste and coal in an industrial-scale circulating fluidized bed boiler. Energy Fuel 31, 14248–14261.

Xu, W., Zhong, W., Zhou, G., et al., 2024. Optimization of air distribution and coal blending in pulverized coal boilers for high-temperature corrosion prevention based on POD reduced-order modeling. Appl. Therm. Eng. 255, 123705.

Yang, K., Li, S., Duan, G., et al., 2024. On fostering predictions in data-driven reduced order model for Eulerian–Lagrangian simulations: decision of sufficient training data. J. Chem. Eng. Jpn. 57, 2316155.

Yang, Y., Ma, H., 2024. A data assimilation pressure field measurement method for linear turbine cascades based on compressed sensing. Phys. Fluids 36, 115174.

Zarepour, M., Bergstrom, D.J., Spiteri, R.J., 2024. Identifying dominant flow structures in a bubbling gas-particle fluidized bed using the spectral proper orthogonal decomposition. Chem. Eng. Sci. 293, 120048.

Zhang, X., Ji, T., Xie, F., et al., 2022. Unsteady flow prediction from sparse measurements by compressed sensing reduced order modeling. Comput. Methods Appl. Mech. Eng. 393, 114800.

Zhao, X., Du, L., Peng, X., et al., 2021. Research on refined reconstruction method of airfoil pressure based on compressed sensing. Theor. Appl. Mech. Lett. 11, 100223.

Zhong, W., Yu, A., Zhou, G., et al., 2016. CFD simulation of dense particulate reaction system: approaches, recent advances and applications. Chem. Eng. Sci. 140, 16–43.